

2. Modeling Small Body Environments

Before motion in the small body environment is studied it is first necessary to define this environment. There exist many different scientific taxonomies for asteroids and comets, and we refer the interested reader to the “Asteroids and Comets” series of texts for a larger view of these bodies [48, 102, 14, 197, 41]. As our focus is on the dynamics of vehicles at these bodies, only a sub-set of all the properties of these bodies needs to be specified. Thus in the following we describe the orbits of small bodies in the solar system, the rotations of these bodies, their gravitational fields and shapes, and the forces that act on a spacecraft or particle in their vicinity.

2.1 Heliocentric and Planetocentric Orbits

Small bodies orbit the sun on trajectories that are dominated by the solar gravitational attraction. The implicit assumption we make in this book is that the orbital motion of a small body can be described accurately by the two-body problem solution. This is an assumption, and is technically not correct as small bodies are subject to additional perturbations that can have significant effects on their motion. These additional perturbations arise from the gravitational attraction of the planets, Jupiter in particular, and from non-gravitational forces acting on the bodies, usually driven by solar irradiation. However, except for some exceptional cases, the assumption that a small body follows an essentially two-body orbit over a timespan of a few orbit periods about the Sun is a good one.

In other situations, when a small body has a close approach to a planet, the interaction between the small body and the planet during the time when they are close to each other can generally be modeled as a hyperbolic orbit. These situations are also important for understanding the effect of a close planetary passage on orbiting particles about a small body. The “interpolation” between these extremes would have the small body subject to two gravitational attractions simultaneously, such as the Trojan asteroids which are attracted by the Sun and Jupiter.

Finally, we make similar assumptions when considering the motion of planetary satellites. For detailed models it is necessary to incorporate perturbations from the

Sun and, in some cases, other satellites about the planet. However, for the general description of their environments over the relatively short time scale considered here the use of a two-body orbital motion suffices.

The initial classifications we focus on are based on the orbits of these bodies. Figures 2.1 and 2.2 graphically display the range of asteroid and comet orbits, and a snapshot of their location in the solar system. The main message from these representations is that the small bodies of the solar system are distributed throughout the solar system, with specific areas of concentration but almost no regions completely devoid of small bodies. Those few that exist arise due to specific perturbations of Jupiter on their orbits, with the best-known regions being the Kirkwood gaps. Figure 2.3 shows a population distribution of asteroids in the Main Belt, clearly indicating the lack of asteroids in regions that are in resonance with Jupiter.

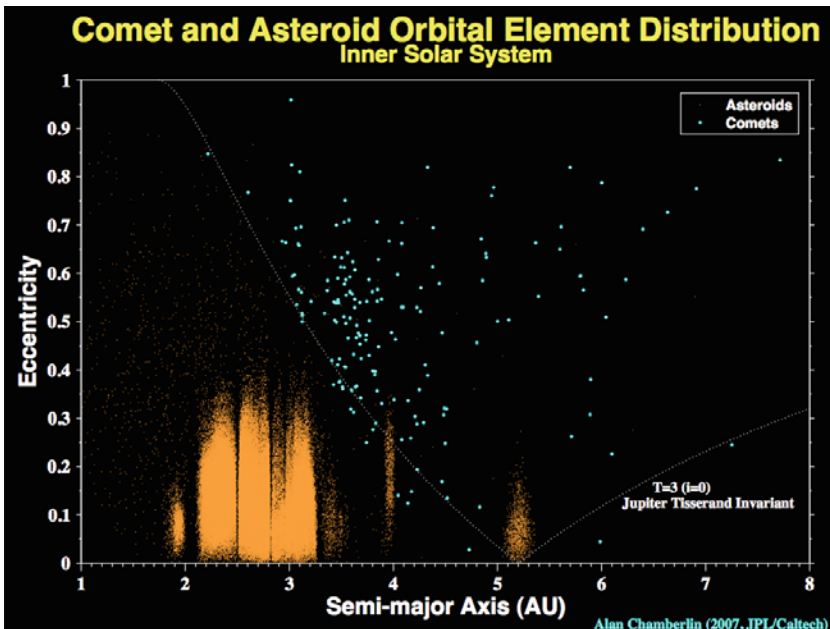


Fig. 2.1 Distribution of semi-major axis and eccentricity for asteroids and comets in the inner Solar System. Credit: Alan Chamberlin, NASA/JPL-Caltech.

2.1.1 Asteroids

Asteroids are found throughout the Solar System and are often discriminated according to their heliocentric orbits. The technical classification of an asteroid is that it is a minor planet and does not exhibit a visible coma or outgassing. This classification can be somewhat ambiguous, with recent controversies over the proper

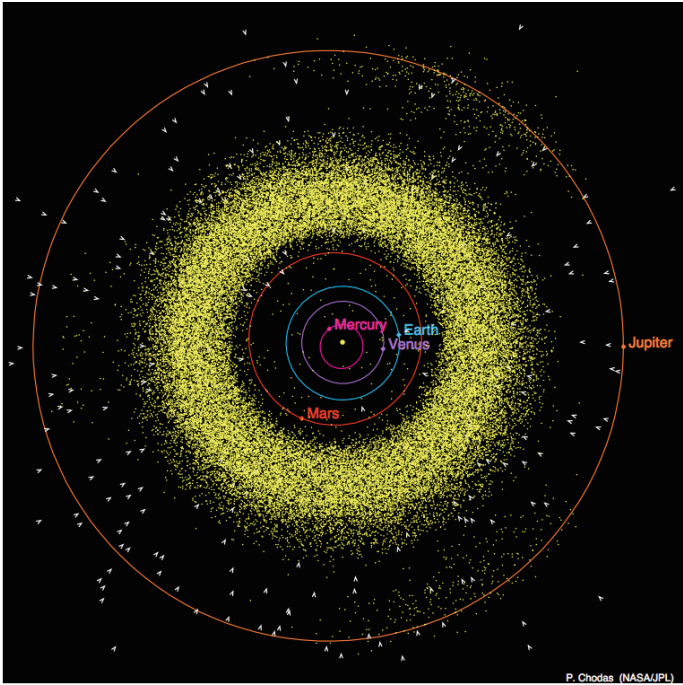


Fig. 2.2 A snapshot of asteroid and comet locations in the inner Solar System. Credit: Alan Chamberlin, NASA/JPL-Caltech.

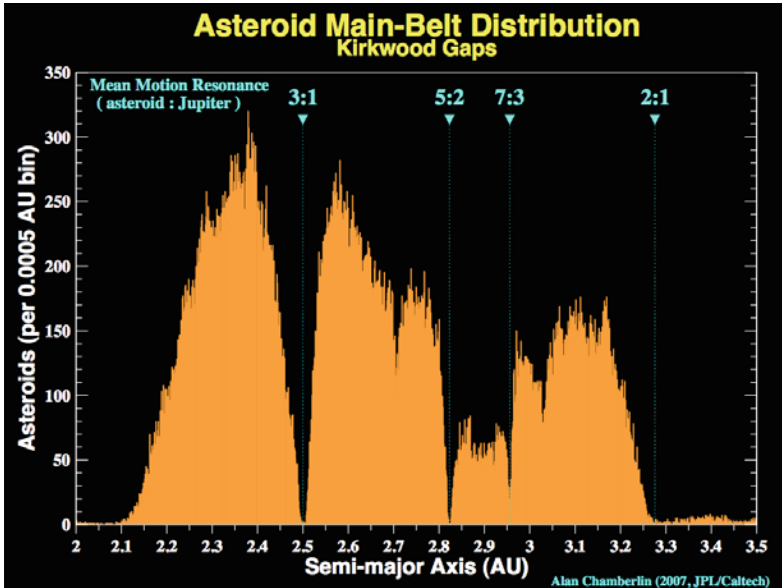


Fig. 2.3 Semi-major axis vs. asteroid population in the Main Belt, clearly showing the Kirkwood gaps. Credit: Alan Chamberlin, NASA/JPL-Caltech.

definition of a planet or dwarf planet, the discovery of some asteroids that seem to undergo periods of outgassing, and a growing realization that there may be a continuum of body types instead of distinct classifications of asteroids and comets. These issues are not of major concern to us here, however.

Near-Earth Objects

The Near-Earth asteroids (NEA) are often classified more generally as Near-Earth Objects (NEO) due to the presence of comet-like bodies that fit into the following orbital definitions. These bodies are clearly distinguished by their heliocentric orbits, as summarized in Table 2.1. NEOs are the most inexpensive bodies to rendezvous with as a class, due to their proximity to the Earth. Certain sub-sets of these bodies have been flagged as potential targets for future human exploration. NEOs are also the bodies with the highest probability of impact with the Earth, and are considered to be objects of interest due to this fact alone.

The lifetime of an NEO has been estimated to be on the order of 10 million years [49], and is limited by their chaotic interactions with the inner planets. These bodies can impact with the terrestrial planets, be ejected from the Solar System, or, most commonly, impact with the Sun. Due to their limited lifetime, there must be a source for these bodies. This source is now known to be the Main Belt, and is described in the following subsection.

Table 2.1 Definitions of Near-Earth Objects from the Near Earth Object Program Office at JPL’s website [178]. q represents perihelion radius, Q represents aphelion radius, P represents orbit period.

Group	Description	Definition
NECs	Near-Earth Comets	$q < 1.3 \text{ AU}$ $P < 200 \text{ years}$
NEAs	Near-Earth Asteroids	$q < 1.3 \text{ AU}$
Atiras	NEAs whose orbits are contained entirely with the orbit of the Earth (named after asteroid 163693 Atira).	$a < 1.0 \text{ AU}$ $Q < 0.983 \text{ AU}$
Atens	Earth-crossing NEAs with semi-major axes smaller than Earth’s (named after asteroid 2062 Aten).	$a < 1.0 \text{ AU}$ $Q > 0.983 \text{ AU}$
Apollos	Earth-crossing NEAs with semi-major axes larger than Earth’s (named after asteroid 1862 Apollo).	$a > 1.0 \text{ AU}$ $q < 1.017 \text{ AU}$
Amors	Earth-approaching NEAs with orbits exterior to Earth’s but interior to Mars’ (named after asteroid 1221 Amor).	$a > 1.0 \text{ AU}$ $1.017 < q < 1.3 \text{ AU}$
PHAs	Potentially Hazardous Asteroids: NEAs whose Minimum Orbit Intersection Distance (MOID) with the Earth is 0.05 AU or less and whose absolute magnitude (H) is 22.0 or brighter.	$\text{MOID} \leq 0.05 \text{ AU}$ $H \leq 22.0$

Main Belt Asteroids

Main Belt asteroids are minor planets primarily found in orbit between Jupiter and Mars. Those observed range in diameter from 948 km (1 Ceres) down to dust detected by interplanetary spacecraft. They are characterized by a strong structure in their semi-major axis distribution, with clear gaps in the population at low-order resonances with Jupiter. The Main Belt is also dominated by families, which are collections of asteroids formed by the impact and break-up of larger bodies. In this sense, the main belt is continually eroding with larger bodies being broken up into cascades of smaller bodies, which themselves impact and continue this fractionation. Due to this the sizes of bodies in the Main Belt are in a collisional distribution, with the number of smaller bodies increasing with a power law with a size dependence on the order of $1/d^{2.3}$. This size distribution is relatively stable, with the largest few asteroids that have survived this process now isolated from other asteroids that could disrupt them, but with impacts continuing among the smaller members. The frequency of family formation is not that rapid, although dynamical astronomers have been able to identify several families that were formed relatively recently in the Main Belt (less than 10 million years ago in one case). [Figure 2.4](#) shows the main groupings within the Main Belt, which to some extent are arranged along major family membership.

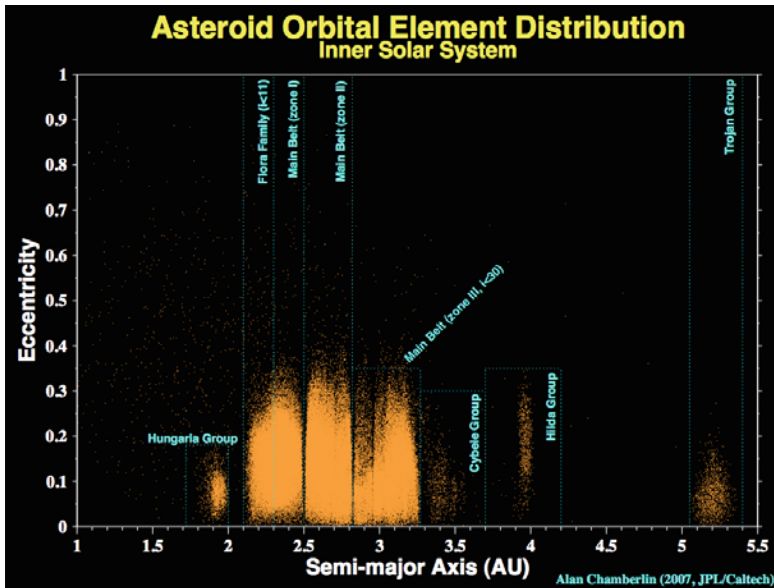


Fig. 2.4 Main asteroid groupings in the inner Solar System. Credit: Alan Chamberlin, NASA/JPL-Caltech.

Collisions between Main Belt asteroids is the main process that modifies and changes these bodies over time, although when one goes to smaller sizes, below 10 km in general, other processes become important and actually serve to migrate

these bodies through the solar system, serving as a source for the NEA. As has been established relatively recently, perturbations from Jupiter can cause asteroids to undergo unstable migrations within the Main Belt and be ejected from the Main Belt. Some of these bodies will scatter into the outer Solar System where interactions with the larger planets can cause these bodies to escape. Others will scatter down into the inner Solar System where they become NEA. A non-gravitational force known as the Yarkovsky effect [144, 25] has been identified as the dominant perturbation on small asteroids in the Main Belt. This effect causes a secular drift in their semi-major axes, allowing them to drift into destabilizing interactions with Jupiter. The Yarkovsky effect arises due to a combination of solar heating of asteroids, thermal inertia of these bodies (which delays the re-emission of absorbed solar photons), and their rotation which ensures that the re-radiated photons have a component that acts normal to the Sun-line. This net component causes a slow drift either towards or away from the Sun depending on the asteroid's obliquity. As it is a non-gravitational effect it preferentially acts on smaller bodies, which is consistent with the small sizes of NEA in general.

Trojans, Centaurs and Beyond

Traditional terminology defines asteroids to include Trojans (bodies captured in Jupiter's 4th and 5th Lagrange points), Centaurs (bodies in orbit between Jupiter and Neptune), and Trans-Neptunian objects (orbiting beyond Neptune). Many of these bodies are expected to be volatile-rich, however, and would likely outgas if they were in closer proximity to the sun. Among these bodies are objects significantly larger than the largest Main Belt asteroid, including the Pluto–Charon system, and thus are more correctly called “minor planets.” The largest Trans-Neptunian objects are over 2,000 km in diameter and have been found to have multiple companions. These minor planets tend to be less rocky and more icy in composition since they formed farther from the Sun. In fact, a group of these objects known as the Kuiper Belt is thought to be the reservoir for short-period comets. The distinction between asteroid and comet has become increasingly difficult to characterize as we learn more about these primordial building blocks of our Solar System. Due to the lack of active outgassing of these bodies, however, a spacecraft in their vicinity would be subject to similar forces as from an asteroid. The major difference arises due to their distance from the Sun and their lower densities.

2.1.2 Comets

Comets are small bodies from the outer Solar System that migrate into orbits which bring them close enough to the Sun so that the volatiles on their surfaces and in their interiors begin to sublimate, causing them to outgas. This causes comets to take on a distinctly different appearance as seen from the Earth, forming large gaseous clouds in their vicinity which are affected by solar photon pressure and form their characteristic tails. The presence of volatiles on comets indicates that they are a pristine reservoir of chemicals and compounds from the formational

epoch of the Solar System. Due to this comets are currently a high scientific priority for both rendezvous missions and eventual sample return missions. The sizes of comets mirror that of asteroids and range from quite small – on the order of kilometers or less – to relatively large bodies up to 100 kilometers. Although comets primarily come from the outer Solar System, the designation of comet is only used for those bodies whose orbits are subsequently perturbed to the extent that their perihelion come close enough to the Sun for visible outgassing. Once such close interactions start, comets have substantial migration of their orbits over their lifetimes. The main force behind their migration is Jupiter, through its gravitational perturbations, and the Sun, through heating and generation of outgassing across their surface. The combination of these gravitational and non-gravitational forces makes it difficult to precisely predict comet orbits and can cause substantial migration over their lifetime. The time scales of these migrations, however, are measured in multiple years whereas the time scales of interest to us are on the order of days and years at most. Thus, it is reasonable for us to neglect changes in the orbits of the bodies studied here.

The primary differences between comets and asteroids are a much lower density for comets and the presence of a gaseous envelope that surrounds these bodies. This envelope is characteristically diffuse when far from the body and is only of dynamical interest when a spacecraft comes into close proximity to the nucleus. A simplistic model for a spacecraft interaction with a cometary jet is presented later in this chapter. The presence of these outgassing jets also perturb comet rotation states, with many of these bodies expected to be in an excited rotation mode. Again, as these are still relatively weak torques the rotational dynamics of these bodies can be modeled as following torque-free excited rotation states, discussed later. Finally, due to their source regions being in the outer Solar System, comet orbits tend to be highly eccentric, as can be seen in [Fig. 2.1](#). This means that solar perturbations acting on orbiters in their vicinity can vary strongly over one orbit period, a consideration explicitly taken into account in our analysis.

For purposes of mission design and spacecraft dynamics, comets can be classified into two main types, short- and long-period comets.

Short-Period Comets

Short-period comets, or more generally periodic comets, are comets that have orbits which repeat in timespans on the order of 200 years or less, or which have been viewed multiple times. The comet Halley is the most famous of this set, and was actually the first comet to be imaged at close range. This class of comets are the usual targets for rendezvous or flyby missions, as their motion is relatively predictable – a crucial aspect for planning space missions.

What is particularly striking about these bodies is that they are transient and change their nature over time. Many comets are expected to eventually go dormant or become extinct, meaning that they no longer show outgassing effects. This can be caused by the depletion of volatiles on or near their surface – the fraction of asteroids that fall into this class is currently unknown. At the other end of the spectrum, they are also sometimes seen to undergo “bursting” following a perihelion

passage, indicating that the outgassing activities on these bodies are substantial enough to erode them and cause them to break apart. Another class of comets have been found that have perihelion extremely close to the Sun, called Kreutz or Sun-grazing comets. This class of comets have been discovered by spacecraft that image the Sun. A common end-state of a body undergoing frequent planetary flybys in the Solar System is that they impact with the Sun. Thus, it is not surprising to find comets with orbits in this state. Due to these different processes all comets currently visible are expected to have finite lifetimes in terms of their visible outgassing activity. This implies that they are replenished from source regions in the outer Solar System.

Within the short-period comets are several sub-classifications. Those specifically mentioned so far include extinct comets, dormant comets, and Kreutz comets. Another classification used is Main Belt comets, which are defined as comets with perihelion within the main asteroid belt. Similarly, Near-Earth comets are comets that satisfy the Near-Earth definitions. Along with these diversity of names are included a diversity of properties, activity levels and even surface morphology.

Long-Period Comets

The other main class of comets are the long-period comets. These are comets that have only been viewed at one apparition. They are on orbits with extremely long periods (technically greater than 200 years but with effective periods up to millions of years), implying that they are on weakly bound, near-parabolic orbits about the Sun and emanate from the Oort Cloud. They can also be classified as inter-stellar comets, meaning that they are not gravitationally bound to the Sun and only have a single apparition before they leave the solar vicinity. These comets are typically found to be quite active and can be very large. Once observed, however, there is generally only a year or two at most until they have their perihelion passage and subsequently go far from the Sun again. Due to this, it is very difficult to plan for a rendezvous mission to such a body. At best, one could implement a flyby mission to such a comet, although the engineering development and approach to such a mission would have to be highly non-standard due to the tight time constraints.

2.1.3 Planetary Satellites

The final class of body considered in this text are planetary satellites. Planetary satellites are found around the majority of planets, only Mercury and Venus have none. Their orbits are generally near-circular, with some notable exceptions, and their orbit planes generally have small obliquities with respect to the heliocentric orbits of their primaries. These bodies are of great scientific interest for a variety of reasons. At one end of the spectrum, the larger planetary satellites – especially those about the gas giants – are thought to have formed via mechanisms similar to the formation of the Solar System’s planets. Thus, their exploration would open new understandings of how these formation processes work. At the other end of the spectrum, some smaller planetary satellites, such as the irregular satellites about

Jupiter and Saturn, are thought to be captured bodies from early in the Solar System's formational process. As such, they may also retain early records of material properties and compositions from the formational epoch of the solar system. Other planetary satellites present challenges for understanding, such as the history of the Martian moons Phobos and Deimos, and the formation of the Moon, which now seems likely to have been formed in a large collision between a Mars-sized protoplanet and the early Earth. Perhaps most intriguing among the planetary satellites are the Jovian moon Europa and the Saturnian moons Titan and Enceladus. Europa and Enceladus are suspected of having liquid oceans trapped beneath their ice-covered shells, and have been identified as potential locations in the solar system where life could have emerged. Titan is now known to have a complex weather system that include methane precipitation and hydrocarbon lakes across its surface.

As a population, the size of planetary satellites range from a few kilometers across to objects larger than the planet Mercury. With only a few exceptions (notably the Martian moons of Phobos and Deimos and some of the smaller satellites of the gas giants) planetary satellites have shapes that are spheroidal, and thus satellite dynamics about these bodies are not affected by their gravity field distributions to the same extent as asteroid orbiters. What makes these strongly perturbed systems are their close proximity to their planets, resulting in significant perturbations from the combined gravitational attraction and centripetal accelerations that they experience due to their orbital motion. Due to these perturbations, whole classes of scientifically attractive orbits about these bodies such as polar orbits can be strongly unstable and present challenges for any space science mission. For a particular example, low-altitude circular polar orbits about Europa can impact with the satellite's surface within a few weeks if not properly designed or controlled. For these reasons a discussion of planetary satellites is included within this book, and the last three chapters are devoted to describing methods for characterizing orbital motion about these bodies.

2.2 Mass and Density of Small Bodies

A fundamental property of a small body is its total mass, as this ultimately controls the gravitational attraction it exerts on a spacecraft. Despite this, once the details of motion around these bodies are explored the total mass of a body is not as crucial of a parameter as its density. The mean density of a body can be computed if the volume and mass is known from $\rho = M/V$, where M is the body mass, ρ is its mean density, and V is its total volume. Another important concept for any body is its mean radius, which is defined as the radius of the sphere of equal volume, or $R = (3V/4\pi)^{1/3}$. By definition, the mean radius is essentially equivalent to the geometric mean of the body's size with the mean radius lying between the maximum and minimum radii of the body. As such, the mean radius is a reasonable measure of how close a spacecraft can come to a given body.

The importance of the density is exemplified if we consider the simple orbit period equation defined by Kepler's 3rd Law

$$T = \frac{2\pi a^{3/2}}{\sqrt{\mathcal{G}M}} \quad (2.1)$$

where T is the orbit period, \mathcal{G} is the gravitational constant, M the body mass, and a the semi-major axis (or orbit radius for a circular orbit). Replacing the total mass using the mean density and mean radius the expression reduces to

$$T = \sqrt{\frac{3\pi}{\mathcal{G}\rho}} \left(\frac{a}{R}\right)^{3/2} \quad (2.2)$$

This shows the well-known result that an orbit period about a body, when specified in terms of body radii, is independent of the body size and only a function of its density. Thus, noting that the Earth's mean density is 5.5 grams per cubic centimeter, an orbit period at the surface of the Earth is 1.4 hours and at one radius altitude is 4 hours. Thus the orbit period about an asteroid of similar density will precisely mirror these periods. This is an important point as it means that the time scale of motion about small asteroids is similar to the same orbit time scales encountered at the Earth, albeit most asteroids have densities on the order of one-half that of the Earth with a commensurate increase of $\sqrt{2}$ in the orbit periods.

It is also instructive to consider the mass scales encountered at asteroids, as these can be directly compared with the spacecraft that visit them. A boulder with mean radius of 1 meter and mean density of 3.5 g/cm³ will have a total mass of approximately 15 metric tons. For comparison, the mass of the NEAR-Shoemaker spacecraft when it was at the asteroid Eros was approximately 0.5 metric tons, or equivalent to a boulder of mean radius 30 centimeters (assuming a mean density of 3.5 g/cm³). Thus, although it is true that small body masses are inconsequential as compared to planetary masses, spacecraft masses are similarly inconsequential as compared to asteroids even a few meters across.

Now consider the measured values of small body density. These are generally difficult measurements to make and require that the body either be a binary system – allowing the total mass to be estimated from Kepler's 3rd Law – or that perturbations to a spacecraft trajectory be measured when in close proximity to the body. As regards to planetary satellites or small binary asteroid secondaries, these can only be estimated if their mass is large enough to cause a measurable reflex motion in the primary. Even the large satellites of Jupiter and Saturn have only been precisely weighed by measuring the deflection of a spacecraft trajectory during close approaches, or by computing their mutual attractions. Comet densities have not been directly measured to date, although they have been estimated to be as low as 0.3 g/cm³. A consistent theme for the estimated densities of asteroids and comets are that measurements have generally found these bodies to have a density significantly less than the density of material they are comprised of. Thus, although the expected grain density of asteroids Eros and Itokawa was on the order of 3.5 g/cm³, the measured bulk densities of these bodies were 2.7 and 2.0 g/cm³,

respectively. Similar results have been found for almost all precisely measured bulk densities, indicating that the internal structure of asteroids has high porosity in general. Based on these measured values, reviewed in [15], it is reasonable to assume bulk densities of between 0.3 and 1 g/cm³ for comets and ranging from 1 to 5 g/cm³ for asteroids. The densities of planetary satellites are not as important, as the perturbations in their vicinity are controlled by several additional factors beyond their mass density, including the mass of their planet and their orbit about the planet.

2.3 Spin States of Small Bodies

Spins are a crucial property of our target bodies as they define how the mass distributions of these bodies vary in inertial space, which controls how they will interact with an orbiting particle. Spin dynamics are easily divided into three classes: uniformly rotating, complex rotation, and synchronized rotation. Asteroids and comets inhabit the first two classes, and planetary satellites almost uniformly inhabit the last. Systems such as binary asteroids can exhibit several types of rotational motion, usually the uniform rotation of the primary and the synchronous rotation of the secondary. Spin states can be determined for asteroids and planetary satellites by observing time variations in the intensity of light scattered from their surface. However, the spin states of comets are not as well known or understood, arising from the difficulty of discriminating between internal light reflection within their comas and variations in reflected light from their surfaces. Still, some comets have had their spin states accurately determined, and we discuss them briefly where appropriate.

Each spin state has unique quantities that will define the body's rotational motion. An important specification shared by all of these spin types is the orientation of their total rotational angular momentum. For the analysis presented in this text a reasonable approximation will be that the bodies conserve their rotational angular momentum. Some exceptions to this occur for planetary satellites and binary asteroid systems, but these will be discussed as appropriate. The usual designation of a body's rotational angular momentum is relative to an inertially fixed frame. Such designations are important for providing a unique classification of a body's rotation; however, for our focus on motion close to these bodies, these inertial coordinates do not provide useful information by themselves. What is more dynamically relevant for our study is the orientation of the body's rotational angular momentum relative to the body's heliocentric (or planetocentric) orbit.

Of prime interest is the orientation of the rotational angular momentum vector, described as a unit vector with two angles relative to the body's orbit. First, define the obliquity of the body as the angle between the heliocentric or planetocentric orbit angular momentum and the rotation angular momentum vectors, denoted as β . Second, denote the right ascension of the body as the orientation of the rotation pole projected into the orbit plane, plus 90°, or geometrically as the planar orientation of the cross product between the orbit normal and the body's angular

momentum vector, denoted as α . As a reference direction in the orbit plane choose the periapsis, denoted as $\hat{\mathbf{E}}$, and the orbit normal, denoted as $\hat{\mathbf{H}}$. The cross product of these defines the triad, $\hat{\mathbf{E}}_{\perp} = \hat{\mathbf{H}} \times \hat{\mathbf{E}}$. With these definitions, the direction of the body's rotational angular momentum is

$$\hat{\mathbf{p}} = \sin \beta \sin \alpha \hat{\mathbf{E}} - \sin \beta \cos \alpha \hat{\mathbf{E}}_{\perp} + \cos \beta \hat{\mathbf{H}} \quad (2.3)$$

2.3.1 Uniform Rotators

The vast majority of asteroids are found to be in a uniform rotation state about their maximum moment of inertia. This is the expected spin state as, under energy dissipation caused by tides raised by complex rotation, it is the minimum energy rotation state of a body [20]. [Figure 2.5](#) shows the size/spin distribution of all asteroids with estimated spin rates and states. Spin rates among uniform rotators range from extremely fast to extremely slow. There is a clear maximum spin rate for larger bodies, equivalent to a spin period on the order of 2.4 hours, evident in [Fig. 2.5](#). This observation has led to the overall realization that larger asteroids are most probably rubble pile bodies, as this limiting spin period equals the spin period when material on the surface of a body with mean density of $\sim 2.1 \text{ g/cm}^3$ enter orbit. This maximum spin rate clearly increases for smaller-sized bodies. Current hypotheses that attempt to explain this are either that smaller bodies are monolithic rocks or that these smaller bodies may still be rubble piles but are bound together with cohesive bonds [133, 69, 169].

Uniform rotators can be specified with a given rotation period or rotation rate and their rotation pole, which is coincident with their rotational angular momentum. Given this, the attitude of a uniformly rotating body can be found by a simple integration of the constant rotation rate. The spin rates and spin poles of asteroids and comets are known to change over time. For asteroids the culprit is the YORP effect [145] while for comets it is torques due to outgassing [150]. The study and analysis of these longer-term dynamics are of interest, but are not relevant over the shorter timespans of interest for spacecraft missions design.

2.3.2 Complex Rotators

There is also a sizable population of asteroids and comets in non-uniform rotation, often referred to as “tumbling” or “complex rotation”. Despite the frequent perception that such bodies are chaotically spinning, they actually follow a well-defined quasi-periodic rotational motion which is described in the next chapter. Larger bodies that are in a complex rotation state generally have a low overall spin rate. This has been clearly related to their relaxation time [63], with estimates for these bodies to relax to uniform rotation about their maximum moment of inertia shown in [Fig. 2.5](#). At the small size scale there is a more puzzling set of tumbling bodies: fast spinners which are in complex spin states. A clear theoretical explanation for the existence or persistence of these bodies has not been fully worked out as of yet, but would present a unique challenge to a rendezvous mission to one of these

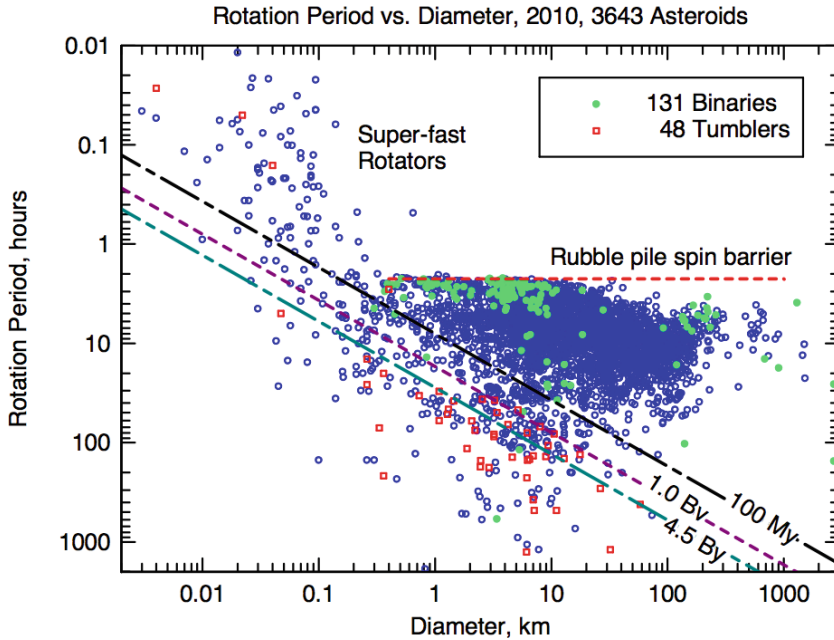


Fig. 2.5 Size–spin period distribution for asteroids. The smaller bodies are almost all in the NEO population with the larger bodies almost all in the Main Belt population. The dashed lines are the expected relaxation times for asteroids in non-principal-axis rotation. Credit: A.W. Harris, personal communication.

bodies. While the number of verified asteroids in non-principal-axis rotation are somewhat modest, the actual population of bodies in complex rotation states may be much larger due to the difficulty in detecting and confirming a non-principal-axis spin state based on light curve observations.

The spin state of a complex rotator is more difficult to specify. There are two fundamental frequencies that appear in their rotational motion, related to their nutation and to the spin rate of the body. Specifying these two quantities is not enough to provide a detailed description of the spin state in time, however. For that the moments of inertia of the body need to be specified as well (or at least the ratios of the moments of inertia). The detailed formula relating spin rates, attitudes and moments of inertia are provided in the next chapter.

2.3.3 Synchronous Rotators

The third distinct class of rotation states are those that are synchronous relative to their mutual orbit with their parent body. For asteroids this class is often found among binary asteroids, where the smaller member is frequently found in a synchronous rotation. In a fraction of binary asteroids synchronicity is also found between both bodies. Planetary satellites are almost all uniformly found in synchronous spin states. The most notable exception to this is the Saturnian moon

Hyperion, which is known to be in chaotic rotation. In a few larger systems, such as Pluto–Charon, the entire system is also doubly synchronous.

Such synchronicity is an expected dynamical state for bodies in orbit about each other. When they are non-synchronous, tides are raised on either body and act to de-spin the smaller body (or both bodies if they have relatively equal size). Eventually this leads them to be trapped into a 1:1 spin–orbit resonance, possibly with some libration. The continued dissipation of energy due to relative motion should eventually damp out this libration, or reduce it to a small value. The one binary asteroid imaged at high resolution, 1999 KW4, showed evidence that the secondary was librating, and thus these bodies are not necessarily completely relaxed to a synchronous state. On the other hand, capture into a synchronous rotation state is presumed to be the fastest tidal dissipation process in binary systems [50], and thus is the expected rotation state of asteroid binary secondaries.

The spin state of a synchronous rotator is specified by the orbit period of the system. If the body is in libration, the maximum libration angle of the satellite relative to the line connecting the two bodies should also be given. Alternatively, the orbit of the system may also be elliptic, which then creates a libration between the satellite and the body centers, even if the satellite spins at a constant rate. The detailed dynamics of interaction of a librating synchronous satellite can be relatively complex, involving interactions between the orbit eccentricity and the forced and free libration of the satellite.

2.4 Size, Shape and Morphology

Asteroids and comets are frequently defined by their shapes, whereas larger planetary satellites generally have shapes that only deviate slightly from spheroids. Thus, our focus is mainly on asteroids and comets in this section. As will be seen later, the detailed surface structure of these bodies is complex with unresolved variations down to the highest resolution at which they have been imaged. This level of fine detail is only needed if the surface motion of a vehicle is modeled. For gravitational and orbital studies, it is sufficient to have lower resolution models that capture the global morphology of a body’s shape without providing the fine details of its surface. Such models are available from NASA’s Planetary Data Systems–Small Bodies Node (PDS-SBN) [117].

2.4.1 Shape Model Formats

There are three fundamental formats that can be found at the PDS-SBN for describing specific shape models. Historically, use was made of a simple tabulation of radius, latitude and longitude, usually with equally spaced longitudes leading to oversampling of the polar regions. Such model formats are still available for some shapes, but this description is not amenable to our work and is not discussed any further. The most versatile shape models are specified as general polyhedra with triangular facets at the surface defined by vertices specified as vectors from a cen-

tral origin. Each facet of the surface can be uniquely modeled as a flat plate for a triangular facet. These shapes can be specified with two lists, one an ordered list of all vertices of the body expressed as vectors in a body-fixed frame, the other being vertex number triples that define the vertices involved with each surface facet. The defining vertices for a facet are generally given in counter-clockwise direction so that the resulting normal defined by the right-hand rule points away from the surface. From Euler's formula there is a simple relation between the number of faces for a triangular facet polygon, f , and the number of vertices, v , where $f = 2(v - 2)$. Thus, to specify a shape model with f triangular facets fully requires $3v = 3(f/2 + 2)$ real numbers and $3f$ integers, or $9f/2 + 6$ total numbers. Due to this, storage requirements for high-resolution shape models can become onerous. Figure 2.6 shows an example model with surface faceting clearly shown.

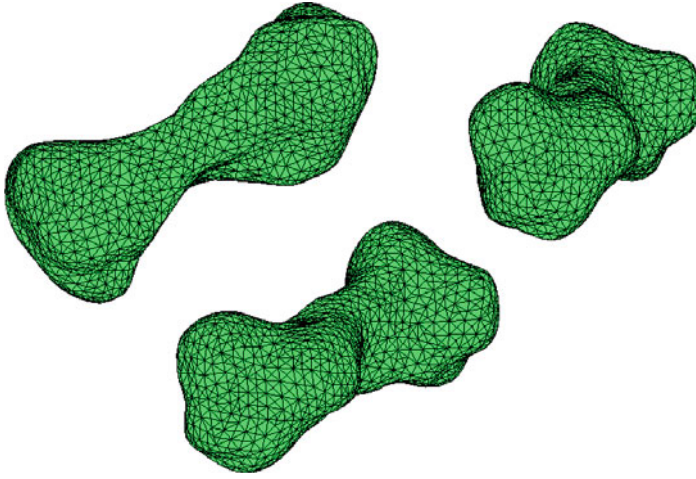


Fig. 2.6 Three views of asteroid Kleopatra in the polygon shape model format, with triangular surface facets.

The third format is the quadrilateral-implied format developed by R.W. Gaskell and also stored in the PDS-SBN for some models. This format describes each surface element of a shape by four vertices. Due to this, the surface cannot be modeled as a flat plate and, indeed, there is some ambiguity in the surface orientation. As the finest surface element is always at or beyond the limit of modeling resolution, it is appropriate to choose some reasonable rule for the surface orientations. Common choices are to define a diagonal between two vertices, splitting the quadrilateral into two triangular segments, or implementing an interpolation routine for the orientation of the surface normal across the body. The model format can be best envisioned as a parallelepiped drawn to enclose the body with the surface of each discretized into n squares on a side, creating $f = 6n^2$ facets. The shape can then be defined by conforming this structure onto the true surface, distorting the grid as necessary in 3-D space to make it cover the surface and account for non-convex surface features (see Fig. 2.7). Since the topology of the surface is fixed, to define the shape one only needs to know the vertices listed in the appropriate order, and

the total number of faces on an edge. Thus, to fully specify a Gaskell shape model one needs a total of $6n^2 + 2$ vertices. Since the shape format is defined implicitly, it is necessary to only have one file listing the vertices in the appropriate order with a header given the number of sides n . Thus, a shape model with a total of f surface facets requires storage of $18f + 12$ real numbers, a factor of four times more than the triangle plate format. However, there are still significant advantages to this form as it is not necessary to search through lists to find facets due to their implied storage. Due to this, it is possible to practically develop shape models of much higher resolution using this approach.

2.4.2 Shapes Based on High-Resolution Imagery

These are the most accurately determined shapes, as they are constructed from combining visual imagery taken at different viewing geometries and phase angles. The best shape models are those constructed from an orbiting spacecraft, as full coverage of the body at a uniform resolution is possible. Only asteroids Eros and Itokawa have shapes with uniformly high resolution as only these two asteroids have been visited by a rendezvous spacecraft to date. The two Mars satellites, Phobos and Deimos, have global shape models but have non-uniform surface resolution, due to flyby constraints for Mars orbiters. Flyby targets can sometimes have global

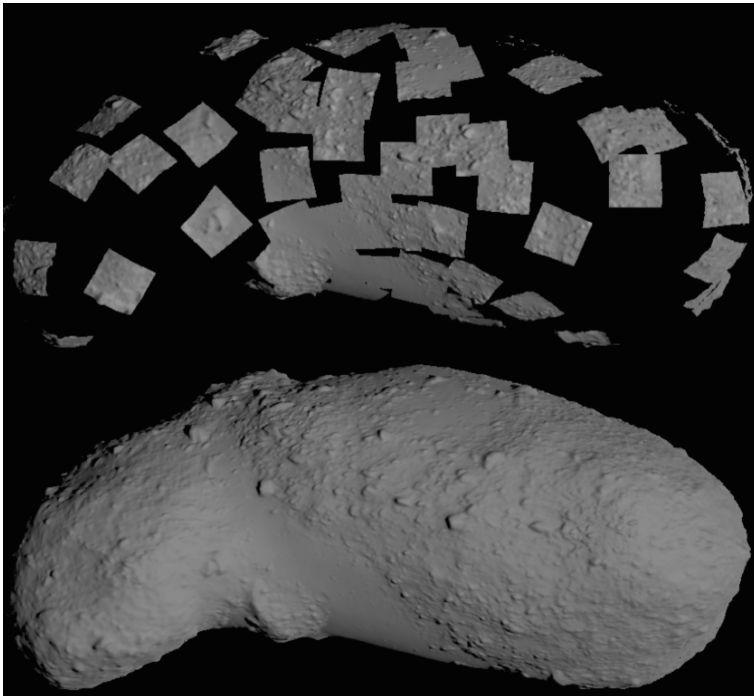


Fig. 2.7 Transitional and final shape model construction for the asteroid Itokawa based on Hayabusa imaging data [44].

shapes, but they are always non-uniform in resolution due to the rapid speeds at which flybys occur. Figure 2.7 graphically shows an intermediate step in the process of shape reconstruction based on asteroid imaging, in this case for asteroid Itokawa.

Shape models for specific bodies imaged by spacecraft are available at the PDS-SBN. These currently include full and partial shapes of asteroids and planetary satellites Phobos, Deimos, Gaspra, Ida, Eros, Mathilde, Itokawa, Lutetia, and Steins. Shape models of Vesta and Ceres will become available as the DAWN mission progresses. Partial comet shape models are also available, or will be soon, for comets Borrelly, Wild 2, Tempel 1 and Hartley 2.

2.4.3 Shapes Based on Radar Range-Doppler Imaging

Based on the pioneering work of Steve Ostro and Scott Hudson, small bodies that pass close enough to the Earth (generally much less than 0.1 AU) and with the proper trajectory can be imaged by the Arecibo or Goldstone radio antenna. During flyby range-Doppler imaging of asteroids can be obtained, and in a complex process the shape and spin state of that body can be estimated [120]. Shape models with surface resolution of less than ten meters have been obtained by this approach, although more typical resolutions are on the order of several tens of meters or larger. The best results also rely on the presence of light curve data for precise determination of the spin period. Shape models for these bodies have usually been produced in the triangular facet model format. Again, shape models for these asteroids are available at the PDS-SBN and currently include Castalia, Toutatis, Kleopatra, Betulia, 1999 KW4 Alpha and Beta, plus several additional ones. Figure 2.8 shows

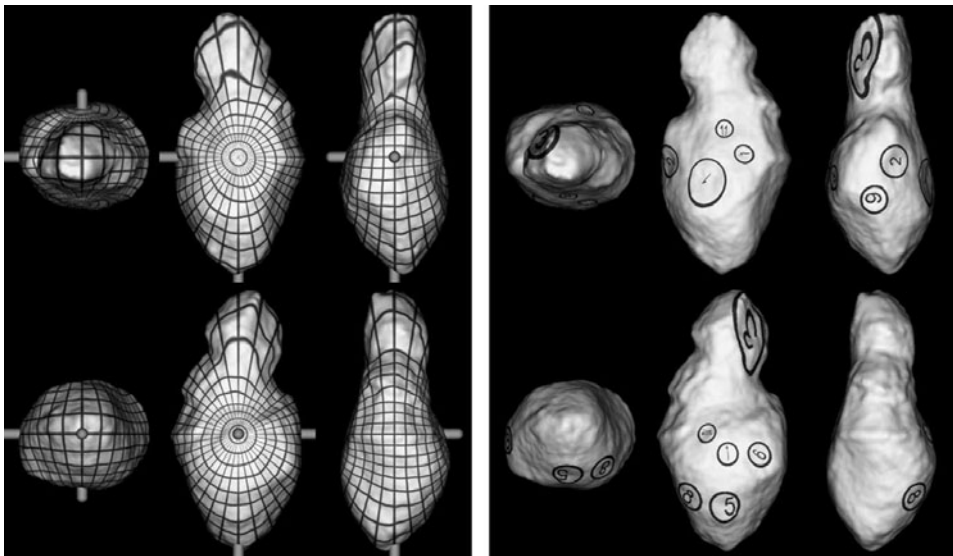


Fig. 2.8 High-resolution shape model of asteroid Toutatis based on its 1996 apparition [77].

the highest global resolution shape model estimated for an asteroid to date using this methodology, with surface resolution at the order of six meters.

2.4.4 Shapes Based on Light Curve Analysis

The simplest manner in which to estimate an asteroid or comet shape is by observing their light curves. These are photometric observations of a body sampled over extended observing periods. This allows the observer to measure the variation in the reflected light. Given an assumed albedo (i.e., reflectance) these measurements also allow the total projected area of the body to be tracked as a function of time. The simplest approach is to map the total variation in reflected light to an upper bound on the ratio between maximum and minimum ellipsoidal axes of the body. Newly developed techniques also enable a convex hull shape to be estimated [78, 79]. Although the resulting information does not provide great detail, it is sufficient to construct an estimate of the asteroid's second degree and order gravitational field, which plays the most significant role in controlling the dynamical evolution of a particle in orbit about the body.

2.4.5 Surface Characteristics

Precision observations of asteroid and comet surfaces are limited. Rendezvous missions have provided local observations of surfaces down to the centimeter scale over specific regions of the bodies, and globally to decimeter scale at Itokawa and meter scale at Eros. These are the highest-quality observations, as the surfaces are generally observed from multiple phase angles, which allow for stereo photoclinometry techniques [46] to determine albedo and surface topography simultaneously. Flyby observations have much lower resolution and generally only one view of the surface. Radar observations provide global surface features at the decameter scale. Resulting from these observations are a few important facts. First, most asteroids and comets have relatively relaxed surfaces, meaning that the vast majority of their surfaces are below the typical angle of repose for granular material, approximately 40 degrees, with many of these bodies having most of their surfaces significantly below slopes of 30 degrees. This relative smoothness does not extend down to small scales, however, as surfaces have strong segregation of surface morphology, with boulders dominating in some regions and others covered with apparent smooth pebbles or dust (in the case of Eros). The boulder terrains are rugged with steep small-scale slopes, while the covered regions generally have low slopes. On Itokawa there is evidence that the smooth regions migrated to their current locations, indicating that the surface of that body may be geologically active [108]. The distribution of material across asteroid surfaces seems to be controlled by the body's geopotential including gravity and rotation effects. Spin rates on some bodies can be fast enough to reverse the usual geopotential lows (which lie at the short axes of a non-rotating ellipsoid) and cause the long axes or equators of the bodies to be the potential low [57].

Comet surfaces have been viewed from a number of flyby missions, and will be investigated in situ once the Rosetta spacecraft has its rendezvous with comet Churyumov-Gerasimenko. The hallmark of comet surfaces are that each seems to be different from the last. Some surfaces, such as for comet Wild 2, have extremely rugged terrain while others, such as comet Tempel 1, have large regions of their surface apparently covered with smooth material. Our understanding of these bodies is still advancing and is likely to change in the future.

2.4.6 Mass Distribution Morphology

A significant and frequent morphology found among asteroids is that they form binary, or in some cases tertiary or higher, systems. Based on measurement statistics it is believed that at least 15% of NEOs are binary objects, with similar percentages being found in the small Main Belt population [135]. Binary asteroids are also very common among larger asteroids and are ubiquitous in the Kuiper Belt. The formation circumstances of binaries are believed to be quite different across the entire range of these bodies and is an active area of research. The modeling of these bodies can also be rather complex depending on the body's detailed circumstances [38], although this text adopts a relatively simple approach to their modeling that captures the main aspects of these bodies of relevance to spacecraft visits.

A different aspect of mass distribution morphology is in regard to the internal density distribution of an asteroid. The one asteroid whose shape and gravity field have been precisely measured to date, Eros, was found to have a large degree of homogeneity in its internal density distribution, with no detectable mass concentrations [107, 83]. This was a somewhat surprising result, and may not be true of all small bodies. In particular, the binary asteroid 1999 KW4 had a statistically significant difference in the density of the smaller and larger components, with the smaller component approximately 40% more dense. A key question for future missions to small asteroids will be to precisely determine the internal density distribution. Unfortunately the gravity field measurements of Itokawa were not of sufficient accuracy to provide strong constraints for that body.

2.5 Gravitational Potentials

The key distinguishing features of small bodies are their irregular shapes, as noted above, and hence their strongly non-spherical mass distributions. This feature drives many of the interesting dynamics when close to these bodies.

The following derivation and discussion assumes that the attraction is between a massless particle and an arbitrary mass distribution. To set up the potential for this situation, we integrate the potential of a differential mass element over the entire body

$$U(\mathbf{r}) = \mathcal{G} \int_B \frac{dm(\boldsymbol{\rho})}{|\mathbf{r} - \boldsymbol{\rho}|} \quad (2.4)$$

where ρ is the position vector of the differential mass element dm , \mathcal{B} is the collection of all mass elements, and \mathcal{G} is the gravitational constant, taken to equal $6.673 \times 10^{-8} \text{ cm}^3 \text{ g}^{-1} \text{ s}^{-2}$. Figure 2.9 shows the geometry of the mass distribution. It can be shown that the gravitational potential satisfies Laplace's equation outside of the body, $\nabla^2 U = 0$, and Poisson's equation inside the body, $\nabla^2 U = -4\pi\mathcal{G}\sigma$ where σ represents the local density. For a sphere with constant density, total mass M , and radius R , integration of this potential yields:

$$U = \begin{cases} \frac{\mathcal{G}M}{|\mathbf{r}|} & r > R \\ \frac{\mathcal{G}M}{2R^3} (3R^2 - r^2) & r \leq R \end{cases} \quad (2.5)$$

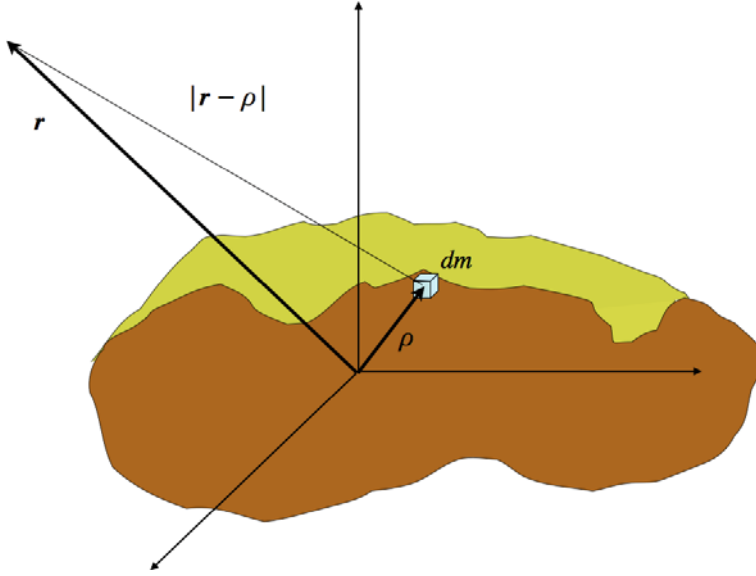


Fig. 2.9 Mass distribution geometry.

2.5.1 Spherical Harmonics Models

There are several approaches to specify the gravitational potential for a non-spherical body. Mathematically, any solution to Laplace's equation which corresponds to the physical mass distribution will work. This fact can be used to great benefit by constructing a set of orthogonal solutions to Laplace's equation and choosing the coefficients of these expansions to match with the actual potential function.

Specifically, Laplace's equation can be solved by separation of variables in terms of spherical coordinates [80]. Denote the spherical coordinates corresponding to a position vector $\mathbf{r} = x\hat{\mathbf{x}} + y\hat{\mathbf{y}} + z\hat{\mathbf{z}}$ as

$$r = \sqrt{x^2 + y^2 + z^2} \quad (2.6)$$

$$\sin \delta = \frac{z}{r} \quad (2.7)$$

$$\tan \lambda = \frac{y}{x} \quad (2.8)$$

where δ is the latitude and λ is the longitude. The general form for the spherical harmonic potential for a gravity field is then:

$$U(r, \delta, \lambda) = \frac{\mu}{r} \sum_{l=0}^{\infty} \sum_{m=0}^l \left(\frac{r_o}{r}\right)^l P_{lm}(\sin \delta) [C_{lm} \cos m\lambda + S_{lm} \sin m\lambda] \quad (2.9)$$

where $\mu = \mathcal{G}M$, the gravitational parameter of the body, r_o is the normalizing radius (often chosen as either the maximum radius or mean radius of the body), P_{lm} are the Associated Legendre Functions, and C_{lm} and S_{lm} are called the gravity field harmonic coefficients (or Stokes coefficients). Specification of these coefficients is analogous to defining the mass distribution and the potential of the body. The Associated Legendre Functions can be defined by the closed-form relationship [80]

$$P_{lm}(\sin \delta) = \cos^m \delta \sum_{i=0}^{\text{int}[(l-m)/2]} T_{lmi} \sin^{l-m-2i} \delta \quad (2.10)$$

$$T_{lmi} = \frac{(-1)^i (2l-2i)!}{2^l i! (l-i)! (l-m-2i)!} \quad (2.11)$$

where the $\text{int}[x]$ function returns the integer part of x (see Appendix E for a partial list of these functions).

Functional orthogonality is an important property of the spherical harmonic expansion. Define the quantity S_{lmi} for $i = 0, 1$ as

$$S_{lm0} = C_{lm} P_{lm}(\sin \delta) \cos(m\lambda) \quad (2.12)$$

$$S_{lm1} = S_{lm} P_{lm}(\sin \delta) \sin(m\lambda) \quad (2.13)$$

Then the orthogonality property is most easily stated as

$$\int_{\delta=-\pi/2}^{\pi/2} \int_{\lambda=0}^{2\pi} S_{lmi} S_{h kj} \cos \delta \, d\delta \, d\lambda = \frac{4\pi(l+m)! \delta_i^j \delta_m^k \delta_h^l}{(l-m)!(2l+1)(2-\delta_m^0)} \quad (2.14)$$

where δ_i^j is the Kronecker delta function and equals 0 if $i \neq j$ and equals 1 if $i = j$. Thus, the integral is only non-zero if all three of the indices match with each other.

If a mass distribution is given, the gravity coefficients C_{lm} and S_{lm} can be directly computed using the orthogonality relations. Specifically, assume that the

density of the body is specified at each point as $\sigma(\boldsymbol{\rho})$. Then the gravity coefficients can be found from the integrals [110]:

$$(C, S)_{lm} = \frac{(2 - \delta_m^0)}{M} \frac{(l - m)!}{(n + m)!} \int_{\mathcal{B}} \left(\frac{r}{r_o} \right)^l P_{lm}(\sin \delta) \text{cs}(m\lambda) \sigma dV \quad (2.15)$$

$$\sigma dV = \sigma(r, \delta, \lambda) r^2 \cos \delta dr d\delta d\lambda \quad (2.16)$$

where r_o is an arbitrary reference radius often taken to equal the maximum radius of the body or the mean radius of the body, and cs denotes the cosine or sine function for computation of the C_{lm} or S_{lm} gravity coefficient, respectively. The reference radius r_o ensures that the gravity coefficients are dimensionless numbers, otherwise they would have units of length to the l th power.

For a constant density body one integration can be performed over the radius and the formula can be reduced to:

$$(C, S)_{lm} = \frac{\sigma(2 - \delta_m^0)}{M} \frac{(l - m)!}{(n + m)!} \int_S \frac{R^3(\delta, \lambda)}{l + 3} \left(\frac{R(\delta, \lambda)}{r_o} \right)^l P_{lm}(\sin \delta) \text{cs}(m\lambda) \cos \delta d\delta d\lambda \quad (2.17)$$

where the radius $R(\delta, \lambda)$ is now a function of the latitude and longitude and defines the shape of the body.

Gravity Coefficients and Mass Moments

There is a well-known relationship between the gravity coefficients of all degrees and orders and the high-order mass distribution moments of an arbitrary body [95]. Of most interest are these relationships up to degree and order 2. First note that $C_{00} = 1$, from the above relationships. Next, note that the first degree and order gravity coefficients are related to the center of mass of the body. Specifically, in the Cartesian coordinates defined by the spherical coordinate system the following relations hold

$$x_{CM} = C_{11} r_o \quad (2.18)$$

$$y_{CM} = S_{11} r_o \quad (2.19)$$

$$z_{CM} = C_{10} r_o \quad (2.20)$$

where x_{CM} , etc. denote the center of mass of the body in the chosen body-fixed coordinate system. It is always possible to redefine the origin of the body-fixed coordinate system to coincide with the center of mass of the body, and thus render the first degree and order terms identically zero, $C_{11} = S_{11} = C_{10} = 0$. For a specified gravity field this is usually done, meaning that the first term beyond the spherical attraction of the body arise at the second degree and order. It is important to note that the center of mass and center of figure of a body will coincide if the body has a constant density distribution. For space missions to small bodies this assumption

is usually made initially; however, subsequent tracking of a spacecraft close to the body can determine whether any first degree and order gravity coefficients exist. If they do, they are evidence of internal density heterogeneity [107, 83].

The second degree and order gravity coefficients are related to the moments of inertia of the body.

$$I_{xx} - I_{yy} = -4Mr_o^2 C_{22} \quad (2.21)$$

$$I_{yy} - I_{zz} = Mr_o^2 (C_{20} + 2C_{22}) \quad (2.22)$$

$$I_{zz} - I_{xx} = -Mr_o^2 (C_{20} - 2C_{22}) \quad (2.23)$$

$$I_{xy} = -2Mr_o^2 S_{22} \quad (2.24)$$

$$I_{yz} = -Mr_o^2 S_{21} \quad (2.25)$$

$$I_{zx} = -Mr_o^2 C_{21} \quad (2.26)$$

These results hold independent of internal density heterogeneity. There are a few important observations that can be drawn from these relations. First, it is not possible to uniquely specify the moments of inertia given the second degree and order gravity coefficients, at best one can only solve for the differences between them. This is an important limitation, as it is often possible to measure the gravity field of an object by tracking its motion, but it is not possible to determine its full moments of inertia from this information. In general, to determine the full moment of inertia the body must also have non-trivial rotational dynamics (i.e., non-principal-axis rotation). The second observation is that for any given mass distribution it is always possible to define a set of coordinates such that the products of inertia, i.e., I_{xy} , I_{yz} , and I_{zx} , are zero. Thus, it is always possible to define a coordinate frame where the second degree and order gravity coefficients $C_{21} = S_{21} = S_{22} = 0$, or that the second degree and order gravity field can be reduced to the two gravity coefficients C_{20} and C_{22} . Again, for a space mission where the gravity field is to be estimated, a usual initial assumption is to choose the coordinate frame fixed in the small body to be nominally aligned with the constant density principal axes. Then, estimation of any non-zero values for the gravity coefficients C_{21} , S_{21} or S_{22} is again evidence of density heterogeneity.

Thus the simplest form of the gravitational potential begins at the second degree and order with only the coefficients C_{20} and C_{22} . Note that in the literature the gravity field coefficient C_{20} is often equivalently specified as the “ J_2 ” gravity coefficient, with the relationship $C_{20} = -J_2$. Then, the simplest, non-trivial gravity field for studying dynamics in the vicinity of a body is:

$$U = \frac{\mu}{r} \left[1 + \left(\frac{r_o}{r} \right)^2 \left\{ C_{20} \left(1 - \frac{3}{2} \cos^2 \delta \right) + 3C_{22} \cos^2 \delta \cos(2\lambda) \right\} \right] \quad (2.27)$$

It has also been found in previous studies that the second degree and order gravity field accounts for the majority of the perturbations on the dynamical system, and thus this model can be taken as a simple stand-in for a more general system.

Limitations of the Spherical Harmonics Approach

The spherical harmonics approach to modeling an arbitrary gravitational field does not work in all situations. A fundamental assumption for the use of this modeling approach are that the series converge to the true gravity field. This assumption appears nowhere in the above statements, but can be identified when one derives the explicit expansion for the gravity field. Consider the general statement of the gravity field again, making a constant density assumption for convenience:

$$U = \frac{\mu}{V} \int_{\mathcal{B}} \frac{dV}{|\mathbf{r} - \boldsymbol{\rho}|} \quad (2.28)$$

To place this function into the form of the spherical harmonic expansion make the assumption that $|\mathbf{r}| > \max_{\mathcal{B}} |\boldsymbol{\rho}|$, meaning that the potential at the point in question lies completely outside the maximum radius of the mass distribution being considered. Under this assumption the integrand can be expanded into the classical Laplace series form

$$\frac{1}{|\mathbf{r} - \boldsymbol{\rho}|} = \frac{1}{r} \sum_{i=0}^{\infty} \left(\frac{\rho}{r}\right)^i P_{i0} \left(\frac{\mathbf{r} \cdot \boldsymbol{\rho}}{r\rho}\right) \quad (2.29)$$

where the P_{i0} are known as the Legendre polynomials (see Appendix E). As detailed in [95] there is a one-to-one correspondence between the integral

$$\frac{1}{V} \int_{\mathcal{B}} \left(\frac{\rho}{r}\right)^i P_{i0} \left(\frac{\mathbf{r} \cdot \boldsymbol{\rho}}{r\rho}\right) dV \quad (2.30)$$

and the i th degree and order spherical harmonic gravity field. If the point in question lies at a radius less than the maximum radius of the mass distribution the Laplace series is not defined when integrating at radii $|\boldsymbol{\rho}| = r$ and diverges when $|\boldsymbol{\rho}| > r$.

A direct remedy for this situation is to define two different expansions, one valid for the usual case when $|\boldsymbol{\rho}| < r$ and the following expansion when $|\boldsymbol{\rho}| > r$:

$$\frac{1}{|\mathbf{r} - \boldsymbol{\rho}|} = \frac{1}{\rho} \sum_{i=0}^{\infty} \left(\frac{r}{\rho}\right)^i P_{i0} \left(\frac{\mathbf{r} \cdot \boldsymbol{\rho}}{r\rho}\right) \quad (2.31)$$

If a finite density is assumed, then the contribution of the gravity field at precisely $r = |\boldsymbol{\rho}|$ vanishes. If this expansion is integrated over the mass distribution outside of radius r another solution of Laplace's equation can be found as a polynomial in r . Generally the coefficients of this external expansion are not used as when the test point radius moves within the maximum radius of the mass distribution, the gravity coefficients of each expansion become a function of the radius r , meaning that they must be recomputed as r changes as the mass distributions being integrated over change. This functional relationship means that the gravity coefficients must then be computed and tabulated at each radius. Recent work has been performed on such interior expansions, reported in [192].

These limitations mean that the usual spherical harmonic expansion cannot be used when considering the gravitational potential close to a small body with irregular shape. It is interesting to note that for an ellipsoid with eccentricities limited to less than $1/\sqrt{2}$, the external gravitational potential will converge [8]. This convergence is fragile and does not survive if the shape is distended sufficiently from a sphere or ellipsoid, and is discussed in more detail in [193]. For a general body the divergence is severe once one comes within the circumscribing sphere of the body (sometimes called the Brillouin sphere, see Fig. 2.10) and makes the gravitational potential essentially worthless for dynamical computations.

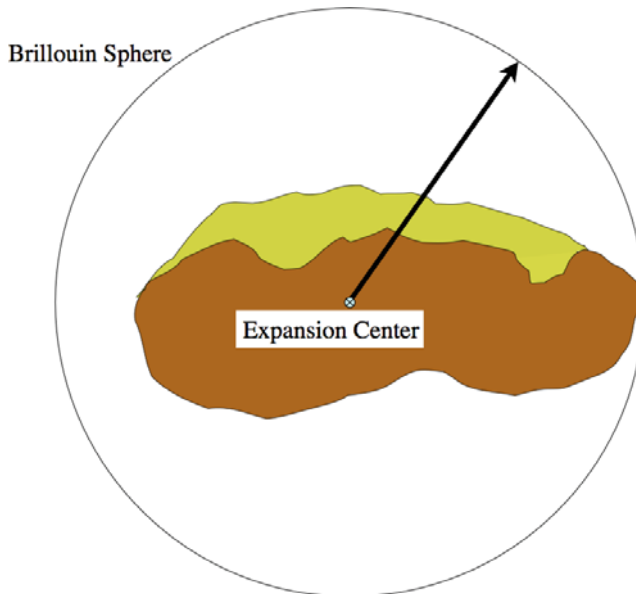


Fig. 2.10 Illustration of the circumscribing sphere about a body, otherwise known as the Brillouin sphere.

One innovative approach to remedying this situation while still using an expansion is the use of ellipsoid harmonic expansions to model the gravitational field, studied and applied to the small body gravitational potential problem in [43]. While ellipsoidal harmonic expansions suffer the same convergence problems, they are mitigated to some degree by having the circumscribing ellipsoid define the boundary between convergence and divergence of the external series. When on or close to the surface there are still divergence issues, but the potential can in general be used much closer to the surface. The cost of this approach is the complexity involved with the computation of the ellipsoidal harmonics orthogonal functions. Ultimately, if one wishes to describe the environment on the surface of a small body this approach also fails.

2.5.2 Closed-Form Gravitational Potentials

To circumvent this limitation there are a number of approaches that rely on the existence of a specified shape for the body in question and strong assumptions on density distribution. The ideal approach to this problem is to find a closed-form solution to Laplace's equation. There are several classical solutions to this problem that can be applied to the gravitational potential problem. At simplest, the sphere with a radially-varying density distribution has a known solution, similar in form to the point mass potential. Of more interest are the closed-form solutions for the constant density ellipsoid and the constant density polyhedron. These have been used in the majority of studies of motion close to and on the surface of small bodies. As exact solutions, they are valid up to and on the surface of the shape in question. They also satisfy Poisson's equation inside of the bodies, which is the analog to the gravitational potential inside of a mass distribution. The definition of these potentials is given in the following.

Constant Density Ellipsoid

Consider a constant density ellipsoid with semi-major axes $\gamma \leq \beta \leq \alpha$. Then the shape of this body is defined by the equation $(x/\alpha)^2 + (y/\beta)^2 + (z/\gamma)^2 \leq 1$ (Fig. 2.11). The total mass of a constant density ellipsoid is $M = 4\pi/3\sigma\alpha\beta\gamma$ and $\mu = \mathcal{G}M$.

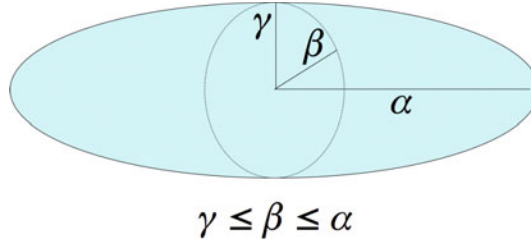


Fig. 2.11 Tri-axial ellipsoid.

The gravitational potential of the exterior region can be found by an application of Ivory's Theorem [112]. Without derivation the ellipsoidal gravitational potential is defined as

$$U(\mathbf{r}) = -\frac{3\mu}{4} \int_{\lambda(\mathbf{r})}^{\infty} \phi(\mathbf{r}, u) \frac{du}{\Delta(u)} \quad (2.32)$$

$$\phi(\mathbf{r}, u) = \frac{x^2}{\alpha^2 + u} + \frac{y^2}{\beta^2 + u} + \frac{z^2}{\gamma^2 + u} - 1 \quad (2.33)$$

$$\Delta(u) = \sqrt{(\alpha^2 + u)(\beta^2 + u)(\gamma^2 + u)} \quad (2.34)$$

where the parameter $\lambda(\mathbf{r})$ is defined by the equation $\phi(\mathbf{r}, \lambda) = 0$. This equation is equivalent to a cubic polynomial and λ is defined to be the maximum real root, which will always exist. The position vector \mathbf{r} is specified in the principal axis frame with the x -axis along the long axis α , y along the intermediate axis β , and z along the short axis γ . The partial derivatives of this potential with respect to the coordinates can be computed by applying Leibniz's rule:

$$U_x = -\frac{3\mu x}{2} \int_{\lambda(\mathbf{r})}^{\infty} \frac{du}{(\alpha^2 + u)\Delta(u)} \quad (2.35)$$

$$U_y = -\frac{3\mu y}{2} \int_{\lambda(\mathbf{r})}^{\infty} \frac{du}{(\beta^2 + u)\Delta(u)} \quad (2.36)$$

$$U_z = -\frac{3\mu z}{2} \int_{\lambda(\mathbf{r})}^{\infty} \frac{du}{(\gamma^2 + u)\Delta(u)} \quad (2.37)$$

The term λ_x does not appear as the integrand is, by definition, zero when evaluated at λ . These terms can no longer be ignored when computing the second partials of the potential. Doing so yields

$$U_{xx} = -\frac{3\mu}{2} \int_{\lambda(\mathbf{r})}^{\infty} \frac{du}{(\alpha^2 + u)\Delta(u)} + \frac{3\mu x^2}{(\alpha^2 + \lambda)^2 \Delta(\lambda)} \frac{1}{\left[\frac{x^2}{(\alpha^2 + \lambda)^2} + \frac{y^2}{(\beta^2 + \lambda)^2} + \frac{z^2}{(\gamma^2 + \lambda)^2} \right]} \quad (2.38)$$

$$U_{yy} = -\frac{3\mu}{2} \int_{\lambda(\mathbf{r})}^{\infty} \frac{du}{(\beta^2 + u)\Delta(u)} + \frac{3\mu y^2}{(\beta^2 + \lambda)^2 \Delta(\lambda)} \frac{1}{\left[\frac{x^2}{(\alpha^2 + \lambda)^2} + \frac{y^2}{(\beta^2 + \lambda)^2} + \frac{z^2}{(\gamma^2 + \lambda)^2} \right]} \quad (2.39)$$

$$U_{zz} = -\frac{3\mu}{2} \int_{\lambda(\mathbf{r})}^{\infty} \frac{du}{(\gamma^2 + u)\Delta(u)} + \frac{3\mu z^2}{(\gamma^2 + \lambda)^2 \Delta(\lambda)} \frac{1}{\left[\frac{x^2}{(\alpha^2 + \lambda)^2} + \frac{y^2}{(\beta^2 + \lambda)^2} + \frac{z^2}{(\gamma^2 + \lambda)^2} \right]} \quad (2.40)$$

$$U_{xy} = \frac{3\mu xy}{(\alpha^2 + \lambda)(\beta^2 + \lambda)\Delta(\lambda)} \frac{1}{\left[\frac{x^2}{(\alpha^2 + \lambda)^2} + \frac{y^2}{(\beta^2 + \lambda)^2} + \frac{z^2}{(\gamma^2 + \lambda)^2} \right]} \quad (2.41)$$

$$U_{xz} = \frac{3\mu xz}{(\alpha^2 + \lambda)(\gamma^2 + \lambda)\Delta(\lambda)} \frac{1}{\left[\frac{x^2}{(\alpha^2 + \lambda)^2} + \frac{y^2}{(\beta^2 + \lambda)^2} + \frac{z^2}{(\gamma^2 + \lambda)^2} \right]} \quad (2.42)$$

$$U_{yz} = \frac{3\mu yz}{(\beta^2 + \lambda)(\gamma^2 + \lambda)\Delta(\lambda)} \frac{1}{\left[\frac{x^2}{(\alpha^2 + \lambda)^2} + \frac{y^2}{(\beta^2 + \lambda)^2} + \frac{z^2}{(\gamma^2 + \lambda)^2} \right]} \quad (2.43)$$

The parameter $\lambda = \lambda(\mathbf{r})$ is always a function of the position vector, this dependency has been suppressed for conciseness in the above.

The computation of the ellipsoidal gravity field appears to be somewhat challenging, given its general formulation as an integral. However, the necessary terms to be computed uniformly fall into the general form of functions known as Carlson's Elliptic Integrals, as summarized (with associated computational algorithms) in [136]. Further, these can be re-expressed in terms of the Jacobi elliptic integrals of the first and second kind. In practice, computation as Carlson's Elliptic Integrals is numerically the most robust approach and can be rapidly evaluated to specified degrees of precision.

Due to the symmetry in an ellipsoid's shape, the gravitational coefficients of its spherical harmonic expansion taken about its center of mass have a relatively simple form. First, all S_{lm} coefficients are identically equal to zero. Second, all coefficients C_{lm} such that either l or m are odd are equal to zero as well. Thus, the only non-zero gravity coefficients are those of the form $C_{2l,2m}$, $l, m = 0, 1, 2, \dots$. In [8] an explicit formula for the ellipsoid's gravity field coefficients are given, with the first few terms specified as:

$$C_{20} = \frac{1}{5r_o^2} \left(\gamma^2 - \frac{\alpha^2 + \beta^2}{2} \right) \quad (2.44)$$

$$C_{22} = \frac{1}{20r_o^2} (\alpha^2 - \beta^2) \quad (2.45)$$

$$C_{40} = \frac{15}{7} (C_{20}^2 + 2C_{22}^2) \quad (2.46)$$

$$C_{42} = \frac{5}{7} C_{20} C_{22} \quad (2.47)$$

$$C_{44} = \frac{5}{28} C_{22}^2 \quad (2.48)$$

Constant Density Polyhedron

In a series of papers Werner detailed closed-form solutions for arbitrary constant density polyhedra [190, 193, 191]. Although the potential is given in closed form, the specific computations necessary to implement this potential are complex enough to require computer code to be written. This particular formulation of the gravity potential was used operationally for the NEAR mission, and has been used in a number of studies of the dynamical environment about asteroids. If local density variations are present or specified, it is possible to add additional potential terms to model such density heterogeneity [170].

The following summarizes the results in [193] for an arbitrary polyhedron with triangular faces. Assume such a body is specified, then from the Euler–Descartes formula for a polyhedron with triangular faces specified by v vertices there must be $f = 2v - 4$ faces and $e = 3(v - 2)$ edges. In Werner's approach the polyhedron is split into its edges and faces. Each face is associated with a set of three vertex vectors \mathbf{r}_i^f , $i = 1, 2, 3$, such that the three vertices taken in order are counter-clockwise about the normal to the face, $\hat{\mathbf{n}}_f$. Associated with each edge e are two vertices \mathbf{r}_i^e ,

$i = 1, 2$, and two faces, f and f' , which join at the edge. Denote the edge normal corresponding to face f as the unit vector $\hat{\mathbf{n}}_e^f$ perpendicular to the edge and to $\hat{\mathbf{n}}_f$ and pointing away from the face center. Thus the edge normals $\hat{\mathbf{n}}_e^f$ and $\hat{\mathbf{n}}_e^{f'}$ point in different directions and are not parallel to each other in general. Given these definitions the general formula for the potential of a polyhedron can be stated as [193]

$$U(\mathbf{r}) = \frac{\mathcal{G}\sigma}{2} \left[\sum_{e \in \text{edges}} \mathbf{r}_e \cdot \mathbf{E}_e \cdot \mathbf{r}_e L_e - \sum_{f \in \text{faces}} \mathbf{r}_f \cdot \mathbf{F}_f \cdot \mathbf{r}_f \omega_f \right] \quad (2.49)$$

$$\frac{\partial U}{\partial \mathbf{r}} = -\mathcal{G}\sigma \left[\sum_{e \in \text{edges}} \mathbf{E}_e \cdot \mathbf{r}_e L_e - \sum_{f \in \text{faces}} \mathbf{F}_f \cdot \mathbf{r}_f \omega_f \right] \quad (2.50)$$

$$\frac{\partial^2 U}{\partial \mathbf{r}^2} = \mathcal{G}\sigma \left[\sum_{e \in \text{edges}} \mathbf{E}_e L_e - \sum_{f \in \text{faces}} \mathbf{F}_f \omega_f \right] \quad (2.51)$$

where \mathbf{r}_e denotes the vector from any point in the edge e to \mathbf{r} and similarly \mathbf{r}_f denotes the vector from any point in the face f to \mathbf{r} . The following terms are defined as

$$\mathbf{E}_e = \hat{\mathbf{n}}_f \hat{\mathbf{n}}_e^f + \hat{\mathbf{n}}_{f'} \hat{\mathbf{n}}_e^{f'} \quad (2.52)$$

$$\mathbf{F}_f = \hat{\mathbf{n}}_f \hat{\mathbf{n}}_f \quad (2.53)$$

$$L_e = \ln \frac{r_1^e + r_2^2 + e_e}{r_1^e + r_2^2 - e_e} \quad (2.54)$$

$$\omega_f = 2 \arctan \frac{\mathbf{r}_1^f \cdot \tilde{\mathbf{r}}_2^f \cdot \mathbf{r}_3^f}{r_1^f r_2^f r_3^f + r_1^f \mathbf{r}_2^f \cdot \mathbf{r}_3^f + r_2^f \mathbf{r}_3^f \cdot \mathbf{r}_1^f + r_3^f \mathbf{r}_1^f \cdot \mathbf{r}_2^f} \quad (2.55)$$

where e_e denotes the actual length of the edge, or $|\mathbf{r}_1^e - \mathbf{r}_2^e|$.

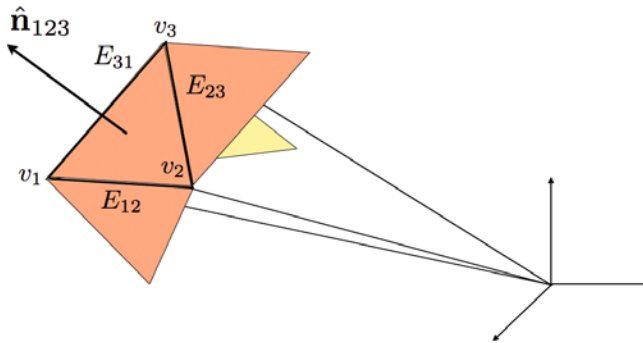


Fig. 2.12 Three vertices, three edges and one surface normal associated with a facet.

The Laplacian of the potential can be shown to be

$$\nabla^2 U = -\mathcal{G}\sigma \sum_{f \in \text{faces}} \omega_f \quad (2.56)$$

The term ω_f denotes the signed area of the face f projected onto the unit sphere centered at the point \mathbf{r} . Thus, when the point is outside of the body the total signed projection equals 0, and when inside the body it equals 4π and thus the polyhedron potential satisfies Laplace’s and Poisson’s equations. Due to this, the potential and partials can be used to compute the gravitational field down to and on the surface of an arbitrary body. Note that, due to this property of the Laplacian of U it is also possible to determine whether a material point is outside or inside of a body by evaluating the Laplacian, thus providing a rigorous manner to determine when impact with a body has occurred.

It is significant to note that closed-form expressions for the spherical harmonic gravity coefficients can be computed given a polyhedron shape model. The procedure and code for performing these computations is detailed in [191]. As the computation of the polyhedron gravity field can be computationally expensive, the use of a spherical harmonic expansion of this field when outside of the circumscribing radius of the body can yield significant computational speed increases. As the harmonic series becomes divergent at the circumscribing sphere, usual practice is to make the transition between polyhedron and spherical harmonic field at a radius larger than the circumscribing sphere.

2.5.3 Other Gravity Field Representations

There are a number of other approximation approaches for the gravitational potential of an arbitrary body that have been used. Most of these use a collection of simple closed-form potential solutions combined in a manner that mimics the gravity field of an actual body. There is scientific heritage for this approach, dating to the use of “mascons” to estimate density inhomogeneities within the lunar gravity field [114]. The most common approach to this problem is to approximate the mass distribution by a collection of point masses. Some past research has taken an existing shape model and filled it with a collection of point masses to mimic the total gravity field. This approach is considered in [193] but shown to be computationally inefficient as compared to the polyhedron model and to provide relatively poor modeling accuracy at the surface of the asteroid. One problem with this approach is that the gravity field of a “cube” of material is modeled as a “sphere”. These two objects have demonstrably different gravity fields when in close proximity leading to systematic errors. The approach was also used by the navigation team for the Hayabusa mission to asteroid Itokawa [101] to approximate the irregular gravity field of that object. The precision of such models are low, however, and it is difficult to uniquely estimate the location and masses of these particles while at the same time finding a robust fit for the true gravity field of an object.

A second approach developed recently is to use the logarithmic potential, which is the gravitational potential of a line element with linear density. There is a simple closed form for these potentials which only involves the use of natural logarithms. By constructing a collection of these it is possible to mimic other gravity fields, especially when point masses are also incorporated. Some relevant research on this topic is reported in [9]. While this can be used to approximately represent a gravity field, no systematic estimation procedure for their placement has been developed as of yet. Thus, their use in practical navigation scenarios is very limited. They are useful for constructing simple systems with which to simulate the dynamical evolution of bodies in non-point-mass potentials.

2.6 Other Forces and Perturbations

When dealing with the orbital motion of a particle in the small body environment the dominant force is usually from the small body gravitational field. Significant perturbations also arise from other gravitational and non-gravitational sources, however. The prime source of these perturbations are the Sun, both gravitational and non-gravitational. Additional sources of perturbation include planetary gravitational perturbations, which could become significant when the small body has a close passage by a planet.

2.6.1 Third-Body Gravitational Perturbations

Solar and planetary gravitational perturbations are simple to specify, if one assumes the small body, or small body system center of mass, lies in a two-body orbit relative to the sun or planet. This is a reasonable approximation, although it tacitly assumes that we will not deal with more complex situations where both planetary and solar gravitational perturbations become significant (which would be a 4+ body problem). The absolute gravitational attraction that a particle would experience is simply $-\left[(\mathcal{G}M_p)/(|\mathbf{r} - \mathbf{d}|^3)\right](\mathbf{r} - \mathbf{d})$ where M_p is the mass of the perturbing body, \mathbf{r} is the vector from the small body center of mass to the particle, and \mathbf{d} is the position vector from the small body center of mass to the perturbing body. In this formulation the sun/perturber is viewed as orbiting the small body, which is only a change of perspective and just implies that the relative position vector goes from the small body to the perturber. The absolute acceleration is not the relevant acceleration to consider for finding the motion of the particle relative to the small body. For that situation the relative or perturbing acceleration is needed, which is just the difference between the absolute acceleration that the particle feels and the absolute acceleration which the small body feels, $+\left[(\mathcal{G}M_p)/|\mathbf{d}|^3\right]\mathbf{d}$, where \mathbf{d} is the position vector of the perturbing body relative to the central body. The

difference of these forms the perturbation gravitational acceleration from a body with mass M_p :

$$\mathbf{a}_p = -\mathcal{G}M_p \left[\frac{(\mathbf{r} - \mathbf{d})}{|\mathbf{r} - \mathbf{d}|^3} + \frac{\mathbf{d}}{|\mathbf{d}|^3} \right] \quad (2.57)$$

For use in perturbation analysis it is convenient to recast this in terms of a perturbing acceleration potential

$$\mathcal{R}_p = \mathcal{G}M_p \left[\frac{1}{|\mathbf{r} - \mathbf{d}|} - \frac{\mathbf{d} \cdot \mathbf{r}}{|\mathbf{d}|^3} \right] \quad (2.58)$$

where

$$\mathbf{a}_p = \frac{\partial \mathcal{R}_p}{\partial \mathbf{r}} \quad (2.59)$$

Of particular note, if the distance between the central body and the perturbing body, d , is much larger than the distance of the particle from the central body, or $d \gg r$, the perturbing potential can be expanded using the Legendre expansion:

$$\mathcal{R}_p = \frac{\mu_p}{d} \left[\sum_{i=0}^{\infty} \left(\frac{r}{d} \right)^i P_{i,0}(\mathbf{r} \cdot \mathbf{d}/rd) - \frac{\mathbf{d} \cdot \mathbf{r}}{|\mathbf{d}|^2} \right] \quad (2.60)$$

From Appendix E the Legendre Polynomial $P_{1,0}(x) = x$, which leads to a cancellation between the $i = 1$ term and the second term in the summation. Also, $P_{0,0}(x) = 1$, and thus the first term of the summation has only a constant contribution. Thus, the perturbation terms that matter do not start until $i = 2$, resulting in the perturbation acceleration:

$$\mathcal{R}_p = \frac{\mu_p}{d} \sum_{i=2}^{\infty} \left(\frac{r}{d} \right)^i P_{i,0}(\mathbf{r} \cdot \mathbf{d}/rd) \quad (2.61)$$

When this expansion is used, usually only the first term is kept. Evaluating this term explicitly, with the Legendre polynomial $P_{2,0}(x) = \frac{1}{2}(3x^2 - 1)$, yields

$$\mathcal{R}_p = \frac{1}{2} \frac{\mu_p}{d^3} \left[3(\mathbf{r} \cdot \hat{\mathbf{d}})^2 - r^2 \right] \quad (2.62)$$

This expansion is the fundamental approximation made in the Hill problem, and will be applied later in this book. It should be noted that the definition of whether \mathbf{d} points from the central body to the perturber or from the perturber to the central body makes no difference in this form of the perturbation. This perturbation, when combined with a rotating reference frame, creates the tidal acceleration discussed in Chapters 12, 17, 18.

If multiple bodies are attracting the spacecraft, a different perturbation potential can be specified for each one, and they can be summed together to create the full potential. It is important to note that the perturbation potential is time-varying

in general, as the position \mathbf{d} varies with time. In this formulation the motion of \mathbf{d} with time can either be supplied from theory, i.e. the two-body solution, or can be provided by an ephemeris.

2.6.2 Solar Photon Perturbation

Also associated with the sun and the heliocentric orbit are non-gravitational perturbations due to momentum transfer from solar photons striking and recoiling off the orbiting body. These non-gravitational forces also act on the small body orbit through the Yarkovsky effect [144], although the relevant timespan involved is many orders of magnitude longer than what interests us here. These same non-gravitational forces also induce a torque on the small body and can modify its rotation state over time, called the YORP effect [145]. Again, the time scale for these are usually much longer than orbital time scales about the small body. If it is desired to incorporate these effects, it is in general sufficient to allow the orbit or rotation state of the small body to change slowly over time without accounting for the rates of change of these quantities in the equations of motion for the orbiting body.

With regard to the spacecraft, the most general and relevant description of these solar forces come from the solar sail literature [103, 140]. From a momentum budget point of view, there are four main contributors to the total force acting on a spacecraft or particle from the incident solar photons. First is the momentum of the impinging photons on the surface. This component acts in the direction of the traveling photons, i.e., along the line from the sun to the particle. Next is the recoil momentum of those photons specularly reflected from the surface. This fraction is found by multiplying the incident radiation by two terms. The first is ρ which is the total reflectance or albedo of the body in question. The next is a factor s which is the fraction of specularly reflected light (i.e., the portion that is like a mirror). Thus the total multiplier is ρs . The direction of the reflected light depends on the local orientation of the surface, with the surface normal bisecting the angle between the incident and specularly reflected light. Third is the recoil momentum of the photons diffusely scattered from the surface. There are two factors involved here, the first being the complement of the specularly reflected light, $\rho(1 - s)$. The second is a scattering coefficient B that describes the fraction of light scattered normal to the surface. For an ideal Lambertian surface this factor is $2/3$, although for a real body this scattering factor will deviate from this ideal value. This reflected light leaves perpendicular to the surface on average, providing an additional momentum transfer against this direction. The final contribution arises from thermal considerations. Of the incident photons, a fraction $(1 - \rho)$ are absorbed by the body and raise its temperature. The body subsequently re-radiates these photons, on average a balance existing between the influx of photons, the temperature of the body, and the outflow of re-emitted photons. For a thin surface the relative emittance of the forward and back surfaces must also be accounted for. The direction of this net momentum transfer is also along the local normal to the surface with its magnitude again decreased by the factor $2/3$ for a Lambertian surface. Finally, the total

radiation pressure of the incident sunlight must be modeled. A typical model is to assume the sun acts as a point source, leading to a simple total pressure:

$$P(d) = \frac{P_0}{d^2} \quad (2.63)$$

where P_0 is a solar constant approximately equal to $1 \times 10^8 \text{ kg km}^3/\text{s}^2/\text{m}^2$. Combined together, the solar radiation force acting on a unit area A is then

$$\begin{aligned} \mathbf{F} = & -P(d) [\{ \rho s (2\hat{\mathbf{n}}\hat{\mathbf{n}} - \mathbf{U}) + \mathbf{U} \} \cdot \hat{\mathbf{u}} \hat{\mathbf{u}} \cdot \hat{\mathbf{n}} \\ & + \{ B(1-s)\rho + (1-\rho)B \} \hat{\mathbf{n}}\hat{\mathbf{n}} \cdot \hat{\mathbf{u}}] H(\hat{\mathbf{u}})A \end{aligned} \quad (2.64)$$

where $\hat{\mathbf{n}}$ is the unit normal to the surface, $\hat{\mathbf{u}}$ is the unit vector from the surface to the sun, and $H(\hat{\mathbf{u}})$ is the visibility function for the surface and is equal to 1 when the sun is in view and 0 otherwise. When summed over all surface elements of the spacecraft and divided by the total mass this yields the net acceleration due to the solar photons.

As opposed to this more complex model, the simplest model for computing solar radiation accelerations is to assume that the spacecraft presents a constant area perpendicular to the sun-line, and that the total momentum transfer is modeled as insolation plus reflection. Then the net acceleration will act away from the sun-line and have the general form

$$\mathbf{a}_{SRP} = -\frac{(1+\rho)P_0 A_{SC}}{M_{SC}} \frac{(\mathbf{d} - \mathbf{r})}{|\mathbf{d} - \mathbf{r}|^3} \quad (2.65)$$

where again \mathbf{d} is the vector from the small body to the sun. An important parameter is the mass to area ratio, denoted here as $B_{SC} = M_{SC}/A_{SC}$, as it controls the relative strength of this perturbation. A typical range of values of B_{SC} for spacecraft is tabulated in [171] and ranges between 20 and 40 kg/m^2 . Spacecraft with large solar arrays will have smaller values of B , and will be more susceptible to these perturbations, which can often be the dominant perturbation for an orbiter.

This simple form of the solar radiation pressure model can be rewritten as a potential

$$\mathcal{R}_{SRP} = -\frac{(1+\rho)P_0}{B_{SC}} \frac{1}{|\mathbf{d} - \mathbf{r}|} \quad (2.66)$$

with $\mathbf{a}_{SRP} = \partial \mathcal{R}_{SRP} / \partial \mathbf{r}$. If the spacecraft is close to the small body, or $r \ll d$, the potential can be further simplified by expanding $1/|\mathbf{d} - \mathbf{r}|$ and keeping the first term that contains the position vector \mathbf{r} .

$$\mathcal{R}_{SRP} = -\frac{(1+\rho)P_0}{B_{SC}} \frac{\mathbf{r} \cdot \mathbf{d}}{d^3} \quad (2.67)$$

with the gradient giving a solar radiation pressure acceleration independent of the spacecraft's position relative to the small body

$$\mathbf{a}_{SRP} \sim -\frac{(1+\rho)P_0}{B_{SC}d^3}\mathbf{d} \quad (2.68)$$

which is often an acceptable approximation for our applications. The magnitude of the solar radiation pressure acceleration is then equal to

$$a_{SRP} = \frac{(1+\rho)P_0}{B_{SC}d^2} \quad (2.69)$$

This model is approximate, but is commonly used to model the non-gravitational accelerations acting on satellites. Higher-precision developments of spacecraft solar radiation pressure or non-gravitational models have been developed [202, 140, 104], and are appropriate for use at a small body. Even with these more general formulations, however, a spacecraft in the vicinity of a small body will frequently be oriented to keep a constant projected area towards the sun to minimize deviations in the non-gravitational perturbations. Thus, in this case it is appropriate to still model the solar radiation pressure as a constant force, perhaps generalized so that the acceleration vector does not necessarily lie along the sun-line.

2.6.3 Comet Outgassing Pressure Models

Finally, a simple model that accounts for the effect of outgassing pressure from a comet acting on an orbiting body is presented. It must be stressed that the detailed modeling and physics of the flow of gases sublimated from the surface of a comet is still an active area of research, and thus the models presented here are simplistic and not grounded in any *in situ* measured comet models. A general description for the construction of comet outgassing models is given in [23], and is summarized here. This model assumes that the outgassing jet emanates from the rotating comet surface and travels radially outwards and expands. Further, the strength of the outgassing jet is a function of the distance of the comet from the sun (which accounts for the total solar insolation on the comet surface) and the relative orientation of the jet site from the sun (which accounts for the relative solar insolation).

The total acceleration felt by an orbiting spacecraft is expressed as

$$\mathbf{a}_J = \frac{\mathbf{p}_0(\mathbf{r}_{SJ})}{B_{SC}} \left(\frac{r_o}{r}\right)^2 \quad (2.70)$$

where \mathbf{p}_0 is the pressure field and direction at the comet surface, \mathbf{r}_{SJ} is the position vector of the spacecraft relative to the center of the jet on the comet surface and r_o is the reference radius of the comet. The parameter B_{SC} is again the spacecraft mass to area ratio, now computed for the spacecraft area exposed to the outgassing jet. This model assumes that the jet strength varies as $1/r^2$ from the comet surface, which may not be particularly valid yet provides a tractable and conservative model

as in reality the drop off may be significantly faster. In the detailed model the pressure field \mathbf{p}_0 spans a cone about the center of the jet; however, for practical computations it often suffices to treat the pressure field as concentrated along a line in space.

A practical implementation of the model specified in [23] is

$$\mathbf{p}_0 = Q_J V_{og} h(\hat{\mathbf{e}}_J \cdot \hat{\mathbf{r}}_J) \hat{\mathbf{r}}_J \quad (2.71)$$

$$h(\hat{\mathbf{e}}_J \cdot \hat{\mathbf{r}}_{SJ}) = \begin{cases} 1 & \hat{\mathbf{e}}_J \cdot \hat{\mathbf{r}}_J > \cos(\delta_J) \\ 0 & \hat{\mathbf{e}}_J \cdot \hat{\mathbf{r}}_J < \cos(\delta_J) \end{cases} \quad (2.72)$$

The angle δ_J is the half-angle of the outgassing jet, as measured from a point on the surface, \mathbf{e}_J is the unit vector defining the direction of the jet relative to the comet surface, $\mathbf{r}_{SJ} = \mathbf{r} - \mathbf{r}_J$ is the relative vector between the spacecraft and the jet's location on the surface of the comet, V_{og} is the speed of the gas as it leaves the surface, and Q_J is a combination of parameters

$$Q_J = S f(\theta_S) g(d) Q_* \quad (2.73)$$

Here Q_* is the mass ejection rate of the comet surface at 1 AU, S is the relative intensity of the comet surface at the jet site, $g(d)$ is a complex function that models the outgassing strength as a function of distance to the sun, and $f(\theta_S)$ computes the relative insolation of the jet site as a function of θ_S , the angle between the jet surface normal and the sun direction. The function form of $g(d_{AU})$ is an empirically derived function taken from [99]

$$g(d_{AU}) = g_0 \left(\frac{d_{AU}}{d_0} \right)^{-c_1} \left[1 + \left(\frac{d_{AU}}{d_0} \right)^{c_2} \right]^{-c_3} \quad (2.74)$$

where $c_1 = 2.15$, $c_2 = 5.093$, $c_3 = 4.6142$, $d_0 = 2.808$ and $g_0 = 0.111262$, and d_{AU} is measured in astronomical units. For the insolation function $f(\theta_S)$ a simple formula can be used

$$f(\theta_S) = \max \begin{cases} 0 \\ 1 - \alpha_J (1 - \theta_S) \end{cases} \quad (2.75)$$

Here α_J is a parameter between 0 and 1 that controls the outgassing strength as a function of solar insolation, and $\cos(\theta_S) = \mathbf{e}_J \cdot \hat{\mathbf{d}}$ is the cosine of the angle between the jet surface normal and the sun. The values for the outgassing parameters vary widely from reference to reference. In [23] the following values are used, $V_{og} = 0.35 \rightarrow 0.95$ km/s and $Q_* = 3.4 \times 10^6$ kg/h, this value varying strongly with the comet in general.

The model presented here is wholly based on a heuristic understanding of comet outgassing jets. It also assumes that the gas velocity is large relative to the speed of the spacecraft relative to the comet, and that the spacecraft is relatively close to the comet. If these are not true, then it is necessary to model the time between

gas ejection and the spacecraft crossing into the jet stream, detailed in [23]. It also assumes that the comet rotation is being modeled, meaning that the inertial location of the vectors \mathbf{r}_J and $\hat{\mathbf{e}}_J$ varies in time with the rotation of the comet.

A simplified form of this model, for use in analytical evaluation, assumes that the jet normal points radially outwards from the center of the comet (modeled as a sphere) and that the crossing of the jet occurs impulsively. Under these approximations the outgassing jet model simplifies to

$$\mathbf{a}_J = \frac{Q_J V_{og}}{B_{SC}} \delta(1 - \hat{\mathbf{r}}_J \cdot \hat{\mathbf{r}}) \frac{\mathbf{r}}{r^3} \quad (2.76)$$

where $\delta(x)$ is the Dirac delta function.

Improved models of comet outgassing are currently under development and will be tested and refined once the Rosetta spacecraft arrives at comet Churyumov-Gerasimenko. A current description of some of these modeling developments can be found in [115]. The main advance in these models is the inclusion of non-radial components of the gas drag, based on sophisticated models of the cometary outgassing process.

<http://www.springer.com/978-3-642-03255-4>

Orbital Motion in Strongly Perturbed Environments
Applications to Asteroid, Comet and Planetary Satellite
Orbiters

Scheeres, D.J.

2012, XVIII, 390 p., Hardcover

ISBN: 978-3-642-03255-4